

Theory for Lattice Relaxation in Marginal Twist Moirés

Christophe De Beule,¹ Gayani N. Pallewela,² Mohammed M. Al Ezzi,³ Liangtao Peng,⁴ E. J. Mele,¹ and Shaffique Adam^{1,4,5}

¹*Department of Physics and Astronomy, University of Pennsylvania, Philadelphia, Pennsylvania 19104, USA*

²*Centre for Advanced 2D Materials, National University of Singapore, 6 Science Drive 2, Singapore 117546*

³*John A. Paulson School of Engineering and Applied Sciences,*

Harvard University, Cambridge, Massachusetts 02138, United States

⁴*Department of Physics, Washington University in St. Louis, St. Louis, Missouri 63130, United States*

⁵*Department of Materials Science and Engineering,*

National University of Singapore, 9 Engineering Drive 1, Singapore 117575

(Dated: March 26, 2025)

Atomically thin moiré materials behave like elastic membranes where at very small twist angles, the van der Waals adhesion energy much exceeds the strain energy. In this “marginal twist” regime, regions with low adhesion energy expand, covering most of the moiré unit cell, while all the unfavorable energy configurations shrink to form topological defects linked by a periodic network of domain walls. We find analytical expressions that successfully capture this strong-coupling regime for both the triangular soliton network and the honeycomb soliton network matching predictions from LAMMPS molecular dynamics simulations, and numerical solutions of continuum elasticity theory. There is an emergent universality where the theory is characterized by a single twist-angle dependent parameter. Our formalism is essential to understand experiments on a wide-range of materials of current interest including twisted bilayer graphene, both parallel and antiparallel stacked tWSe₂ and tMoTe₂, and any other twisted homobilayer with the same stacking symmetry.

Moiré van der Waals materials are stacks of two-dimensional materials where the unit cell is engineered to be much larger than the atomic lattice constant. This is achieved through either a lattice mismatch or a relative rotational twist between two adjacent layers. The expansion of the unit cell acts to target and energetically flatten the lowest energy bands close to the Fermi energy. Over the past six years, such moiré engineering has led to a long list of exciting experimental observations including of superconductivity in twisted bilayer graphene [1] and twisted WSe₂ [2, 3], as well as correlated states like Wigner crystals in WSe₂/WS₂ heterostructures [4], orbital Chern insulators in twisted mono-bilayer graphene [5], and interaction-induced halos in twisted double-bilayer graphene [6].

While it is convenient to think of the constituent layers as rigid crystals, it was soon appreciated both experimentally [7] and theoretically [8–10] that they are more like membranes where “lattice relaxation” arises from competition between intralayer elastic strain that resists relaxation and interlayer van der Waals adhesion energy that wants to expand regions with favorable stacking configurations. The gain in adhesion energy grows as the moiré cell area leading to a reconstruction of the moiré at sufficiently small twists. Often this is an essential ingredient for observed electronic effects. For example, without lattice relaxation the flat bands of magic-angle twisted bilayer graphene near charge neutrality would merge with the higher-energy dispersive bands [11], and there would not be a substrate-induced topological gap [8, 12] that underpins the observation of the orbital quantum anomalous Hall effect [13] in twisted bilayer graphene aligned to a hexagonal boron nitride substrate.

To date, most treatment of lattice relaxation has

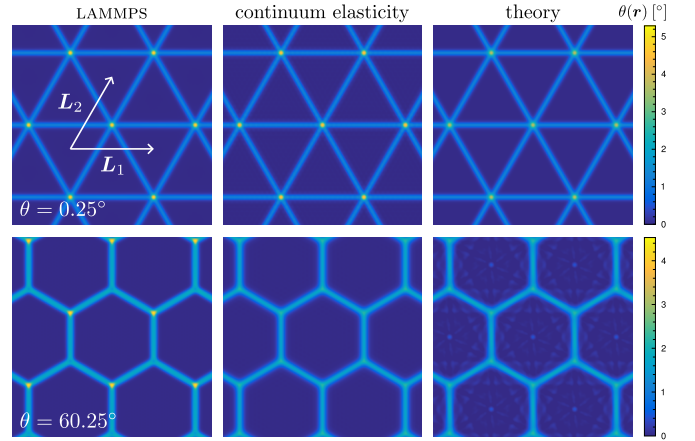


FIG. 1. Comparison of our theory with LAMMPS molecular dynamics simulations and numerical solutions of continuum elasticity. Top: Local twist angle $\theta(\mathbf{r}) = (1/2)\nabla \times \phi(\mathbf{r})$ for a marginal D_6 twist moiré. LAMMPS simulations are for 2H tWSe₂ with $\theta = 0.25^\circ$, continuum elasticity uses $\eta \approx 25.6$, and our theory for a triangular soliton network uses a domain wall slope 0.044. These values are chosen to give the same physical situation. Bottom: Same for honeycomb soliton network with $\theta = 60.25^\circ$, $\eta \approx -5.9$, and domain wall slope 0.060.

been heavily numerical relying on density-functional theory [14–16], LAMMPS molecular dynamics simulations [17–19], or numerical solutions of continuum elasticity [11, 20–24]. These approaches generally work well (and are in agreement) in the weak coupling limit, i.e., for “large” twist angles. Very recently there has also been some analytical progress in this perturbative limit [25–27]. In this Letter, we tackle analytically the opposite limit of strong coupling at small twist angles (the so-called “marginal twist” regime). We find analytical

expressions that successfully match continuum elasticity and molecular dynamics simulations where the only adjustable parameters are exactly the same as those for the large-angle perturbative theory (and therefore easily obtainable from numerical methods). Since our expressions are asymptotically exact for both small and large twist angles, combining them should give a reasonably accurate theory for structural relaxation of twisted hexagonal homobilayers at all angles near 0° or 60° .

Model — In the long-wavelength limit, a bilayer moiré is defined by the local stacking configuration or interlayer registry $\phi(\mathbf{r}) = M\mathbf{r} + \mathbf{u}(\mathbf{r})$ (also called the phason field) [28]. This is the lateral shift between the two layers, which is spatially modulated in a moiré. Here M is a constant 2×2 matrix (displacement gradient) that defines the rigid moiré, and $\mathbf{u} = \mathbf{u}_1 - \mathbf{u}_2$ is the acoustic displacement field due to lattice relaxation, where the subscript labels the two layers. The displacement gradient can include relative rotations, lattice mismatch, and heterostrain [29]. The moiré lattice is then defined by $\mathbf{L} = M^{-1}\mathbf{a}$ where \mathbf{a} is a lattice vector of the monolayer: $\phi(\mathbf{r} + \mathbf{L}) = \phi(\mathbf{r}) + \mathbf{a} \equiv \phi(\mathbf{r})$. In particular, for homobilayer twist moirés, we have $M\mathbf{r} = (a/L)\hat{z} \times \mathbf{r}$ with $L = a/[2\sin(\theta/2)]$ the moiré lattice constant.

When the moiré scale is much larger than the atomic scale, we can treat the layers as continuous membranes and model the acoustic degrees of freedom with continuum elasticity [11]. We further assume that out-of-plane motion is quenched by encapsulation. In this case, the ground state static configuration at zero temperature is obtained by minimizing the energy $F[\phi] = F_{\text{elas}}[\phi] + F_{\text{adh}}[\phi]$ imposing moiré periodic boundary conditions. The first term gives the elastic energy from heterostrain and the second term gives the adhesion energy from the interlayer vdW interaction:

$$F_{\text{elas}}[\phi] = \int d^2\mathbf{r} \left[\frac{\lambda}{4} (\partial_i \phi_i)^2 + \frac{\mu}{8} (\partial_i \phi_j + \partial_j \phi_i)^2 \right], \quad (1)$$

$$F_{\text{adh}}[\phi] = \int d^2\mathbf{r} V[\phi(\mathbf{r})], \quad (2)$$

where μ, λ are monolayer Lamé constants, $V(\phi)$ is the stacking-fault energy or adhesion potential, and summation is implied. This results in a 2D version of the Frenkel–Kontorova model. For twist moirés in particular, the theory is characterized by a coupling constant $\eta = (L^2/a^2)V_1/\mu \approx c_1/\theta^2$ with $c_1 = V_1/\mu$. Here V_1 is the dominant Fourier component of the stacking-fault energy, which sets the energy barrier between favorable and unfavorable stackings.

One then identifies two regimes: a weak coupling “large angle” regime $|\eta| \ll 1$ and a strong coupling “small angle” regime $|\eta| \gg 1$. For weak coupling, we have shown in a recent Letter [25] that the displacement field for twist moirés with D_6 or D_3 symmetry in lowest order is

$$\mathbf{u}(\mathbf{r}) = \frac{\sqrt{3}a|c_1|}{\pi\theta^2} \sum_{i=1}^3 \hat{z} \times \hat{g}_i \sin(\mathbf{g}_i \cdot \mathbf{r} + \psi_i), \quad (3)$$

where $\psi_1 = \arg(c_1)$ with $\psi_1 = 0, \pi$ for D_6 . Here \mathbf{g}_i ($i = 1, 2, 3$) are moiré reciprocal vectors of the first star, related by 120° rotations. This theory can be systematically refined by going to higher order in η [25, 27].

In this work, we instead consider the strong coupling regime and develop an expansion of the displacement field in $1/\eta = \theta^2/c_1$. In this limit, it is well known that domains with near uniform stacking emerge on the scale of the moiré lattice [30, 31], see Fig. 1. These correspond to energetically favorable stacking configurations, while unfavorable ones contract, forming topological defects linked by a periodic network of domain walls (solitons in ϕ). In this regime, the moiré period is much larger than the domain wall width, and $\sqrt{c_1}/\theta$ is exactly the ratio of these length scales [24]. Examples of twist moirés with D_6 stacking symmetry are twisted bilayer graphene ($|c_1| \sim 10^{-5}$), and 2H and 1T homobilayer transition metal dichalcogenides (TMDs) ($|c_1| \sim 10^{-4}$) twisted near 0° and 60° , respectively. While twisting the latter two near 60° and 0° yield structures with D_3 stacking. We note that $c_{1,\text{TMD}}/c_{1,\text{tBG}} \sim 10$ such that the same relaxation physics is expected for $\theta_{\text{TMD}} \approx 3\theta_{\text{tBG}}$.

To gain insight into the strong coupling limit, we consider a first-star theory with D_6 symmetry. Up to an additive constant, $V[\phi] = 2V_1 \sum_{i=1}^3 \cos(\mathbf{g}_i M^{-1} \cdot \phi)$. When $V_1 > 0$, the potential has two degenerate minima denoted as AB and BA stacking ($\phi = \pm a\hat{x}/\sqrt{3}$) and one maxima which we call AA stacking ($\phi = 0$). We note that AA need not correspond physically to eclipsing layers. Because of the Poincaré–Hopf theorem there also exist three saddle points (SP) resulting in a *triangular network* of shear solitons with domain walls that correspond to the SPs. By contrast, when $V_1 < 0$, AA stacking is the only favorable configuration, and one obtains a *honeycomb* network. The latter applies to D_3 structures for $|\eta| \gg 1$. While there are two unfavorable nondegenerate configurations in this case, both contract to a point resulting in an emergent D_6 symmetry.

It is useful to define longitudinal and transverse Fourier components of the displacement field $u_{\mathbf{g}}^{\parallel} = (iL/a)\mathbf{g} \cdot \mathbf{u}_{\mathbf{g}}$ and $u_{\mathbf{g}}^{\perp} = (iL/a)(\hat{z} \times \mathbf{g}) \cdot \mathbf{u}_{\mathbf{g}}$. These give the divergence and curl, respectively. Under a moiré stacking symmetry \mathcal{S} we then find $u_{\mathcal{S}\mathbf{g}}^{\parallel} = \pm u_{\mathbf{g}}^{\parallel}$ and $u_{\mathcal{S}\mathbf{g}}^{\perp} = \pm \det(\mathcal{S})u_{\mathbf{g}}^{\perp}$ with an extra sign when the layers are swapped. Moreover, they are decoupled in the elastic energy density:

$$f_{\text{elas}}(u_{\mathbf{g}}^{\parallel}, u_{\mathbf{g}}^{\perp}) = \frac{a^2}{4L^2} \sum_{\mathbf{g}} \left[(\lambda + 2\mu) |u_{\mathbf{g}}^{\parallel}|^2 + \mu |u_{\mathbf{g}}^{\perp}|^2 \right]. \quad (4)$$

Because twist moirés relax mostly through local untwisting [25, 32] the $u_{\mathbf{g}}^{\perp}$ are dominant. Numerically, we find $|u_{\mathbf{g}}^{\parallel}/u_{\mathbf{g}}^{\perp}| < 10^{-2}$ and therefore set $\lambda = 0$. For a D_6 twist moiré, \mathcal{C}_{6z} yields one real $u_{n,m}^{\parallel}$ and $u_{n,m}^{\perp}$ for each star with representative $n\mathbf{g}_1 + m\mathbf{g}_2$ belonging to the n th shell ($m = 0, \dots, n-1$). Here we define stars as equal length reciprocals closed under \mathcal{C}_{6z} with $\mathbf{g}_1 = 4\pi\hat{y}/3L$ and $\mathbf{g}_2 = \mathcal{C}_{3z}\mathbf{g}_1$. In addition, \mathcal{C}_{2x} gives $u_{n,m}^{\parallel} = -u_{n,n-m}^{\parallel}$

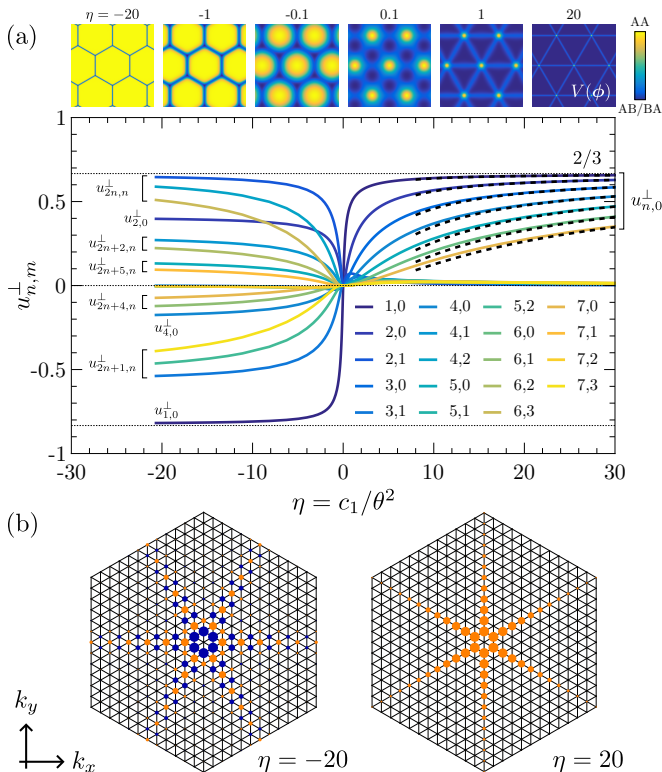


FIG. 2. (a) Transverse components $u_{n,m}^{\perp}$ as a function of $\eta = c_1/\theta^2$ where $m = 0, \dots, n-1$ for stars with representatives $n\mathbf{g}_1 + m\mathbf{g}_2$. We only show distinct values for the first 7 shells. Solid (dashed) lines give results from continuum elasticity (theory). The top panel shows $V[\phi(\mathbf{r})]/V_1$ in real space. (b) Reciprocal structure $u_{\mathbf{g}}^{\perp}$ up to 12 shells (78 stars) for $\eta = \mp 20$ where the dot size and color give the magnitude and sign (orange positive and blue negative).

and $u_{n,m}^{\perp} = u_{n,n-m}^{\perp}$. Hence longitudinal components vanish for stars invariant under C_{2x} .

Triangular soliton network — For the triangular network the shear solitons are partial dislocations (AB/SP/BA) and the *exact* solution is

$$\mathbf{u}(\mathbf{r}) = \frac{\sqrt{3}a}{2\pi} \sum_{i=1}^3 \hat{z} \times \hat{g}_i \sum_{n=1}^{\infty} \frac{u_{n,0}^{\perp}}{n} \sin(n\mathbf{g}_i \cdot \mathbf{r}), \quad (5)$$

where $\mathbf{g}_3 = -\mathbf{g}_1 - \mathbf{g}_2$. This field has support on stars concentric with the first that are all orthogonal to the domain walls and by symmetry $u_{n,0}^{\parallel} = 0$. Consider first the limit $\eta \rightarrow \infty$. Although continuum elasticity breaks down, it is instructive. We find $u_{n,0}^{\perp} \rightarrow 2/3$ and

$$\lim_{\eta \rightarrow \infty} \mathbf{u}(\mathbf{r}) = \frac{a}{\sqrt{3}\pi} \sum_{i=1}^3 \hat{z} \times \hat{g}_i \arctan \left[\cot \left(\frac{\mathbf{g}_i \cdot \mathbf{r}}{2} \right) \right], \quad (6)$$

giving sharp domain walls. The factor $2/3$ is determined by the shift between AA and AB/BA stacking, which is the largest possible displacement. For finite $\eta \gg 1$, the domain walls attain a finite width. We match their slope

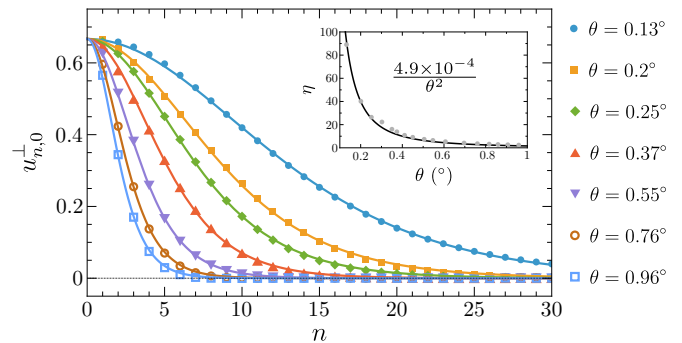


FIG. 3. Dominant Fourier components $u_{n,0}^{\perp}$ obtained from LAMMPS simulations for 2H tWSe₂ and fit to $(2/3) \text{sech}^2 [2n/(3\sqrt{\eta})]$. The inset gives the fitted values of η as a function of twist angle, showing the expected $1/\theta^2$ behavior with a domain wall slope $2\sqrt{c_{1,\text{eff}}} \approx 0.044$.

to that of a single AB/SP/BA domain wall centered at $\mathbf{r}_0 = \sqrt{3}L\hat{y}/2$ [33]. Expanding Eq. (5) in y/L gives

$$\phi(\mathbf{r}_0 + y\hat{y}) - \phi_{\text{SP}} \simeq -\frac{y\hat{x}a}{L} \left(1 + \sum_{n=1}^{\infty} [2 + (-1)^n] u_{n,0}^{\perp} \right), \quad (7)$$

which needs to match the slope $2\sqrt{\eta}a/L = 2\sqrt{c_1}$ of the isolated soliton, as shown in the Supplemental Material (SM) [34]. This is satisfied by

$$u_{n,0}^{\perp}(\theta) = \frac{2}{3} \text{sech}^2 \left(\frac{2n\theta}{3\sqrt{c_1}} \right), \quad (8)$$

among other choices [34]. This function decays exponentially with n and the sum converges for $n_{\text{max}} \approx \eta$.

In Fig. 1 we compare Eq. (5) to both the numerical solution of continuum elasticity and to LAMMPS molecular dynamics simulations with state-of-the-art interatomic potentials [34]. Including second and third star contributions to the adhesion potential modifies the domain wall slope to $2\sqrt{c_1 - 8c_2 + 9c_3}$ with $c_i = V_i/\mu$ [24, 34]. We can capture these contributions within the first-star theory using an effective $c_{1,\text{eff}} = c_1 - 8c_2 + 9c_3$, e.g., for tWSe₂ near 0° we find $c_{1,\text{eff}} \approx 4.88 \times 10^{-4}$ matching approximately the value obtained by extracting the c_i in the large-angle regime [34]. While our theory accurately reproduces the domain wall, the size of the AA region is slightly overestimated because of small contribution from other stars and because Eq. (8) slightly deviates from the (exponentially decaying) numerical values at larger n . Nonetheless we find remarkably good agreement with the numerical solution [see dashed black lines in Fig. 2(a)]. Moreover, in Fig. 3 we show that our *ansatz* for the transverse components fits perfectly LAMMPS simulations for aligned tWSe₂ where the only fit parameter is the slope of the domain wall.

Honeycomb soliton network — In the honeycomb case the solitons are full shear dislocations (AA/SP/AA).

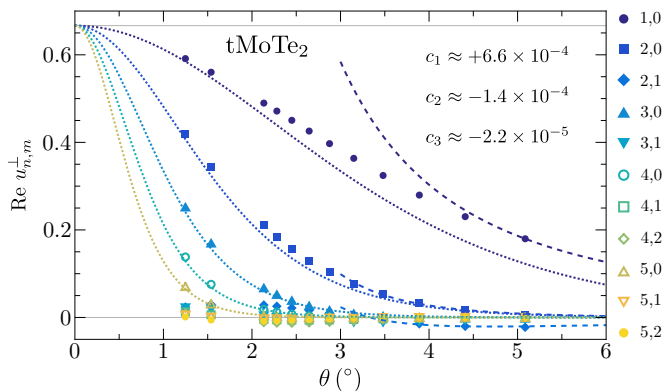


FIG. 4. Real part of transverse Fourier components $u_{n,m}^{\perp}$ of the acoustic in-plane displacement field for tMoTe₂. Data points were obtained from Ref. [35] where machine learning force fields were used together with large-scale density-functional theory calculations. The dashed lines are fits to 2nd order perturbation theory in c_i/θ^2 [34] giving c_1 , c_2 , and c_3 as indicated, and dotted lines show the small-angle theory $u_{n,0}^{\perp} = (2/3) \text{sech}^2 [2n\theta/(3\sqrt{c_{1,\text{eff}}})]$ with *no further adjustable parameters*, i.e., $c_{1,\text{eff}} = c_1 - 8c_2 + 9c_3$.

However, because the network is not primitive, the solution is much more complicated. Unlike for the triangular case, for which there is only one type of dominant contribution, the main contributions for the honeycomb network are due to: (i) $u_{n,0}^{\perp}$ which oscillate between positive and negative and decay rapidly with n , and (ii) three other sets of stars: $u_{2n,n}^{\perp}$, $u_{2n+1,n}^{\perp} = u_{2n+1,n+1}^{\perp}$, and $u_{2n+2,n}^{\perp} = u_{2n+2,n+2}^{\perp}$, see Fig. 2(a). The set $u_{2n,n}^{\perp}$ by itself yields a triangular network scaled by $1/\sqrt{3}$ and rotated by 30° . This gives too many solitons with the wrong slope. The role of the remaining contributions is to remove the extra ones and correct the slope.

As before we can expand $\phi(\mathbf{r})$ near a domain wall $\mathbf{r}_0 = \hat{x}L/2$, retaining only these stars. Setting the slope equal to that of the isolated soliton gives

$$4\sqrt{2|\eta|} \approx 1 + 3 \sum_{n=1}^{\infty} (-1)^n u_{n,0}^{\perp} + \frac{2 + (-1)^n}{3} u_{2n,n}^{\perp} - \frac{(1+2n)[1 + (-1)^n + 2n]}{1 + 3n(1+n)} u_{2n+1,n}^{\perp} + \frac{2(1+n)^2 + (-1)^n(2+2n+n^2)}{2 + 3n(1+n/2)} u_{2n+2,n}^{\perp}, \quad (9)$$

where $4\sqrt{2|c_1|}$ is the slope of an isolated AA/SP/AA soliton [34]. However, because there are multiple contributions, this gives too few conditions. Therefore, we take a different approach. First, we extract the domain wall slope from the LAMMPS simulations which gives an effective η . For tWSe₂ with $\theta = 60.25^\circ$ we find $\eta \approx -5.9$ corresponding to $c_{1,\text{eff}} \approx -1.14 \times 10^{-4}$. We then fit con-

	a	b	r	s
$u_{2n,n}^{\perp}$	0.68	-0.096	0.028	0.64
$u_{2n+1,n}^{\perp}$	-0.59	0.23	0.033	0.69
$u_{2n+2,n}^{\perp}$	0.31	-0.20	0.042	0.69

TABLE I. Parameters for honeycomb soliton network obtained fitting to continuum elasticity for $\eta \in [-25, -10]$ [34].

tinuum elasticity according to

$$u_{n,0}^{\perp} = -0.26 \sin(2.1n) \text{csch}(0.27n), \quad (10)$$

$$u_{2n+i,n}^{\perp} = \left(a_i + \frac{b_i}{\sqrt{|\eta|}} \right) \text{sech}^2 \left[n \left(r_i + \frac{s_i}{\sqrt{|\eta|}} \right) \right], \quad (11)$$

where the parameters are given in Table I. We contrast this to the triangular case where using the same procedure gives $(a, b, r, s) = (0.66, 0, 0.021, 0.55)$. We note that Eq. 8 corresponds to $(a, b, r, s) = (2/3, 0, 0, 2/3)$. While we believe that the values in Table I are similarly related to each other, we have not been able to find such a simplification.

Discussion — To illustrate the power of the analytical theory, we apply our method to twisted bilayer MoTe₂. This is an important example since this material hosts exotic new phases like the fractional quantum anomalous Hall states [35, 36]. Here relaxation is particularly important since it changes the band topology. The experimentally observed Chern number sequence [37] was reproduced by the machine learning force field method of Ref. [35]. To test our theory, we first Fourier transform the acoustic part of the in-plane displacement field obtained from Ref. [35]. This is shown in Fig. 4 where we only show the real part of the transverse components because the imaginary and longitudinal parts are three orders of magnitude smaller. Small imaginary parts are present because D_6 stacking symmetry is only approximate for tTMDs twisted near 0° . Consistent with Fig. 2 the small-angle regime is dominated by $u_{n,0}^{\perp}$ which signals domain formation. We then obtain the parameters $c_i = V_i/\mu$ by fitting the data for large angles to perturbative solutions of continuum elasticity up to 2nd order in c_i/θ^2 [34]. Without further fitting, we compare the data at small twist angles to the analytical theory of Eq. (8) using $c_{1,\text{eff}} = c_1 - 8c_2 + 9c_3$. As shown in Fig. 4, the agreement is remarkable. We emphasize that the effective parameter for small twists is completely determined by the fit at large twist angles.

Our theoretical framework provides analytic expressions for the in-plane center of mass positions in the absence of homostrain, at both large [25] and small (present work) twist angles. Therefore, the effects of lattice relaxation can systematically be included into electronic continuum models [38] previously developed for rigid lattices at high symmetry points, e.g., Refs. [39, 40] for K/K' , and Refs. [41, 42] at the M points. In principle, this will yield accurate fully-relaxed electronic structures

of moiré materials at any twist angle including in the strong-coupling marginal-twist regime.

The solutions presented here are valid for any marginally stacked 2D material where the van der Waals energy landscape has either D_3 or D_6 symmetry. As discussed earlier, this already encompasses a wide range of existing (and yet to be discovered) twisted 2D materials including homobilayers of graphene and TMDs in both parallel and antiparallel stacking configurations. Moreover, the procedure we develop to obtain semi-analytical solutions for the soliton networks should apply to any symmetry, e.g., we speculate that square lattices with D_4 symmetry (e.g. twisted PdSe₂ or GeSn) will behave similarly to the D_6 case studied here with two degenerate minima in the energy landscape yielding only one dominant set of $u_{n,m}^\pm$. This highlights an important aspect of the strong coupling limit – it is governed by a new emergent universality, i.e., models with very different properties and symmetries at large twist angle can behave very similarly at small twist angle. The physical properties depend only on the symmetry of the soliton domain wall network and a single (twist-angle dependent) effective parameter given by the ratio of the moiré length to the domain wall width. Hints of this universality is already present in existing experiments. As seen in Fig. 4, for tTMDs, the strong coupling physics already

becomes important for $\theta \lesssim 3^\circ$. Therefore, it is unsurprising that in this regime DFT predictions deviate strongly from continuum models extrapolated from large twist angles [35, 43]. Moreover, this helps explain the similarity between the quantum spin Hall states observed in both twisted WSe₂ at 3° and MoTe₂ at 2.1° [37, 44]. Since these are both in the strong coupling regime for lattice relaxation, we expect that the electronic properties are universal and governed mostly by the emergent triangular soliton network.

ACKNOWLEDGMENTS

We thank Valentin Crépel and Di Xiao for interesting discussions and Martin Claassen for computational resources. We thank the authors of Ref. [35] for providing us with their full numerical data set. L.P. and S.A. are supported by a start-up grant at Washington University in St. Louis. G.N.P., M.M.A.E., L.P., and S.A. acknowledge support of Singapore National Research Foundation Investigator Award (NRF-NRFI06-2020-0003). M.M.A.E acknowledges Simons Foundation Award No. 896626. C.D.B. and E.J.M. are supported by the U.S. Department of Energy under Grant No. DE-FG02-84ER45118.

-
- [1] Y. Cao, V. Fatemi, S. Fang, K. Watanabe, T. Taniguchi, E. Kaxiras, and P. Jarillo-Herrero, Unconventional superconductivity in magic-angle graphene superlattices, *Nature* **556**, 43 (2018).
 - [2] Y. Guo, J. Pack, J. Swann, L. Holtzman, M. Cothrine, K. Watanabe, T. Taniguchi, D. G. Mandrus, K. Barmak, J. Hone, A. J. Millis, A. Pasupathy, and C. R. Dean, Superconductivity in 5.0° twisted bilayer WSe₂, *Nature* **637**, 839 (2025).
 - [3] Y. Xia, Z. Han, K. Watanabe, T. Taniguchi, J. Shan, and K. F. Mak, Superconductivity in twisted bilayer WSe₂, *Nature* **637**, 833 (2025).
 - [4] Y. Xu, S. Liu, D. A. Rhodes, K. Watanabe, T. Taniguchi, J. Hone, V. Elser, K. F. Mak, and J. Shan, Correlated insulating states at fractional fillings of moiré superlattices, *Nature* **587**, 214 (2020).
 - [5] H. Polshyn, J. Zhu, M. A. Kumar, Y. Zhang, F. Yang, C. L. Tschirhart, M. Serlin, K. Watanabe, T. Taniguchi, A. H. MacDonald, and A. F. Young, Electrical switching of magnetic order in an orbital Chern insulator, *Nature* **588**, 66 (2020).
 - [6] M. He, Y. Li, J. Cai, Y. Liu, K. Watanabe, T. Taniguchi, X. Xu, and M. Yankowitz, Symmetry breaking in twisted double bilayer graphene, *Nature Physics* **17**, 26 (2021).
 - [7] C. R. Woods, L. Britnell, A. Eckmann, R. S. Ma, J. C. Lu, H. M. Guo, X. Lin, G. L. Yu, Y. Cao, R. V. Gorbachev, A. V. Kretinin, J. Park, L. A. Ponomarenko, M. I. Katsnelson, Y. N. Gornostyrev, K. Watanabe, T. Taniguchi, C. Casiraghi, H.-J. Gao, A. K. Geim, and K. S. Novoselov, Commensurate-incommensurate transition in graphene on hexagonal boron nitride, *Nature Physics* **10**, 451 (2014).
 - [8] J. Jung, A. M. DaSilva, A. H. MacDonald, and S. Adam, Origin of band gaps in graphene on hexagonal boron nitride, *Nature Communications* **6**, 6308 (2015).
 - [9] P. San-Jose, A. Gutiérrez-Rubio, M. Sturla, and F. Guinea, Electronic structure of spontaneously strained graphene on hexagonal boron nitride, *Physical Review B* **90**, 115152 (2014).
 - [10] M. van Wijk, A. Schuring, M. Katsnelson, and A. Fasolino, Moiré Patterns as a Probe of Interplanar Interactions for Graphene on h-BN, *Physical Review Letters* **113**, 135504 (2014).
 - [11] N. N. T. Nam and M. Koshino, Lattice relaxation and energy band modulation in twisted bilayer graphene, *Physical Review B* **96**, 075311 (2017).
 - [12] N. Bultinck, S. Chatterjee, and M. P. Zaletel, Mechanism for Anomalous Hall Ferromagnetism in Twisted Bilayer Graphene, *Physical Review Letters* **124**, 166601 (2020).
 - [13] M. Serlin, C. L. Tschirhart, H. Polshyn, Y. Zhang, J. Zhu, K. Watanabe, T. Taniguchi, L. Balents, and A. F. Young, Intrinsic quantized anomalous Hall effect in a moiré heterostructure, *Science* **367**, 900 (2020).
 - [14] G. Cantele, D. Alfè, F. Conte, V. Cataudella, D. Ninno, and P. Lucignano, Structural relaxation and low-energy properties of twisted bilayer graphene, *Physical Review Research* **2**, 043127 (2020).
 - [15] X. Liu, R. Peng, Z. Sun, and J. Liu, Moiré Phonons in Magic-Angle Twisted Bilayer Graphene, *Nano Letters* **22**, 7791 (2022).
 - [16] APS -2024 APS March Meeting - Event - Structural relaxation effects on the low-energy electronic structure

- of twisted bilayer graphene, in *Bulletin of the American Physical Society* (American Physical Society).
- [17] M. H. Naik, I. Maity, P. K. Maiti, and M. Jain, Kolmogorov–Crespi Potential For Multilayer Transition-Metal Dichalcogenides: Capturing Structural Transformations in Moiré Superlattices, *The Journal of Physical Chemistry C* **123**, 9770 (2019).
- [18] A. P. Thompson, H. M. Aktulga, R. Berger, D. S. Bolintineanu, W. M. Brown, P. S. Crozier, P. J. in 't Veld, A. Kohlmeyer, S. G. Moore, T. D. Nguyen, R. Shan, M. J. Stevens, J. Tranchida, C. Trott, and S. J. Plimpton, LAMMPS - a flexible simulation tool for particle-based materials modeling at the atomic, meso, and continuum scales, *Computer Physics Communications* **271**, 108171 (2022).
- [19] N. Leconte, S. Javvaji, J. An, A. Samudrala, and J. Jung, Relaxation effects in twisted bilayer graphene: A multi-scale approach, *Physical Review B* **106**, 115410 (2022).
- [20] S. Carr, D. Massatt, S. B. Torrisi, P. Cazeaux, M. Luskin, and E. Kaxiras, Relaxation and domain formation in incommensurate two-dimensional heterostructures, *Physical Review B* **98**, 224102 (2018).
- [21] D. Bennett, Theory of polar domains in moiré heterostructures, *Physical Review B* **105**, 235445 (2022).
- [22] M. Koshino and N. N. T. Nam, Effective continuum model for relaxed twisted bilayer graphene and moiré electron-phonon interaction, *Physical Review B* **101**, 195425 (2020).
- [23] J. Kang and O. Vafek, Pseudomagnetic fields, particle-hole asymmetry, and microscopic effective continuum Hamiltonians of twisted bilayer graphene, *Physical Review B* **107**, 075408 (2023).
- [24] A. Ramos-Alonso, B. Remez, D. Bennett, R. M. Fernandes, and H. Ochoa, Flat and Tunable Moiré Phonons in Twisted Transition-Metal Dichalcogenides, *Physical Review Letters* **134**, 026501 (2025).
- [25] M. M. A. Ezzi, G. N. Pallewela, C. De Beule, E. Mele, and S. Adam, Analytical Model for Atomic Relaxation in Twisted Moiré Materials, *Physical Review Letters* **133**, 266201 (2024).
- [26] A. Ceferino and F. Guinea, Pseudomagnetic fields in fully relaxed twisted bilayer and trilayer graphene, *2D Materials* **11**, 035015 (2024).
- [27] J. Kang and O. Vafek, [Analytical solution for the relaxed atomic configuration of twisted bilayer graphene including heterostrain](#) (2025), arXiv:2502.15154 [cond-mat].
- [28] H. Ochoa, Moiré-pattern fluctuations and electron-phonon coupling in twisted bilayer graphene, *Physical Review B* **100**, 155426 (2019).
- [29] F. Escudero, A. Sinner, Z. Zhan, P. A. Pantaleón, and F. Guinea, Designing moiré patterns by strain, *Physical Review Research* **6**, 023203 (2024).
- [30] J. S. Alden, A. W. Tsen, P. Y. Huang, R. Hovden, L. Brown, J. Park, D. A. Muller, and P. L. McEuen, Strain solitons and topological defects in bilayer graphene, *Proceedings of the National Academy of Sciences* **110**, 11256 (2013).
- [31] N. Tilak, G. Li, T. Taniguchi, K. Watanabe, and E. Y. Andrei, Moiré Potential, Lattice Relaxation, and Layer Polarization in Marginally Twisted MoS₂ Bilayers, *Nano Letters* **23**, 73 (2023).
- [32] N. P. Kazmierczak, M. Van Winkle, C. Ophus, K. C. Bustillo, S. Carr, H. G. Brown, J. Ciston, T. Taniguchi, K. Watanabe, and D. K. Bediako, Strain fields in twisted bilayer graphene, *Nature Materials* **20**, 956 (2021).
- [33] Q. Gao and E. Khalaf, Symmetry origin of lattice vibration modes in twisted multilayer graphene: Phonons versus moiré phonons, *Physical Review B* **106**, 075420 (2022).
- [34] See Supplemental Material at [insert link] for more details on the methodology employed to solve the equations of motion from continuum elasticity.
- [35] X.-W. Zhang, C. Wang, X. Liu, Y. Fan, T. Cao, and D. Xiao, Polarization-driven band topology evolution in twisted MoTe₂ and WSe₂, *Nature Communications* **15**, 4223 (2024).
- [36] J. Cai, E. Anderson, C. Wang, X. Zhang, X. Liu, W. Holtzmann, Y. Zhang, F. Fan, T. Taniguchi, K. Watanabe, Y. Ran, T. Cao, L. Fu, D. Xiao, W. Yao, and X. Xu, Signatures of fractional quantum anomalous Hall states in twisted MoTe₂, *Nature* **622**, 63 (2023).
- [37] K. Kang, B. Shen, Y. Qiu, Y. Zeng, Z. Xia, K. Watanabe, T. Taniguchi, J. Shan, and K. F. Mak, Evidence of the fractional quantum spin Hall effect in moiré MoTe₂, *Nature* **628**, 522 (2024).
- [38] B. A. Foutty, C. R. Kometter, T. Devakul, A. P. Reddy, K. Watanabe, T. Taniguchi, L. Fu, and B. E. Feldman, Mapping twist-tuned multiband topology in bilayer WSe₂, *Science* **384**, 343 (2024).
- [39] J. M. B. Lopes dos Santos, N. M. R. Peres, and A. H. Castro Neto, Graphene Bilayer with a Twist: Electronic Structure, *Physical Review Letters* **99**, 256802 (2007).
- [40] R. Bistritzer and A. H. MacDonald, Moiré bands in twisted double-layer graphene, *Proceedings of the National Academy of Sciences* **108**, 12233 (2011).
- [41] C. Lei, P. T. Mahon, and A. H. MacDonald, [Moiré band theory for M-valley twisted transition metal dichalcogenides](#) (2024), arXiv:2411.18828 [cond-mat].
- [42] D. Călugăru, Y. Jiang, H. Hu, H. Pi, J. Yu, M. G. Vergniory, J. Shan, C. Felser, L. M. Schoop, D. K. Efetov, K. F. Mak, and B. A. Bernevig, [A New Moiré Platform Based on M-Point Twisting](#) (2024), arXiv:2411.18684 [cond-mat].
- [43] T. Devakul, V. Crépel, Y. Zhang, and L. Fu, Magic in twisted transition metal dichalcogenide bilayers, *Nature Communications* **12**, 6730 (2021).
- [44] K. Kang, Y. Qiu, K. Watanabe, T. Taniguchi, J. Shan, and K. F. Mak, Double Quantum Spin Hall Phase in Moiré WSe₂, *Nano Letters* **24**, 14901 (2024).
- [45] [DIIS convergence acceleration in SCF](#) ().
- [46] P. Pulay, Improved SCF convergence acceleration, *Journal of Computational Chemistry* **3**, 556 (1982).
- [47] J.-W. Jiang, Parametrization of Stillinger–Weber potential based on valence force field model: application to single-layer MoS₂ and black phosphorus, *Nanotechnology* **26**, 315706 (2015).

Supplemental Material for “Theory for Lattice Relaxation in Marginal Twist Moirés”

CONTENTS

S1. Continuum elasticity	S1
A. AB/BA domain walls	S2
B. AA/SP/AA domain wall	S3
C. Soliton slope of triangular network	S4
S2. Numerical solution	S4
A. Self-consistent solution	S4
B. Perturbation theory	S5
C. First-star theory	S7
Numerical implementation	S7
S3. LAMMPS molecular dynamics simulations	S9

S1. CONTINUUM ELASTICITY

We start by deriving the equations of motion governing the disregistry $\phi(\mathbf{r})$ in the absence of out-of-plane corrugations. The equilibrium configuration is obtained from the variational derivative

$$\frac{\delta F}{\delta \phi(\mathbf{r})} = 0, \quad F = \int d^2 \mathbf{r} \mathcal{F}[\phi(\mathbf{r}), \nabla \phi(\mathbf{r})], \quad (\text{S1})$$

which gives

$$\frac{\partial \mathcal{F}}{\partial \phi_i} - \partial_j \frac{\partial \mathcal{F}}{\partial (\partial_j \phi_i)} = 0. \quad (\text{S2})$$

One finds

$$\frac{\partial \mathcal{F}}{\partial (\partial_j \phi_i)} = \frac{\lambda}{2} \delta_{ij} \partial_i \phi_i + \frac{\mu}{2} (\partial_j \phi_i + \partial_i \phi_j), \quad (\text{S3})$$

where repeated indices are *not* summed. This yields [24, 33]

$$2 \frac{\partial V}{\partial \phi} = (\lambda + \mu) \nabla (\nabla \cdot \phi) + \mu \nabla^2 \phi, \quad (\text{S4})$$

with $V[\phi(\mathbf{r})]$ the stacking-fault energy, μ the shear modulus, and $\mu + \lambda$ the bulk modulus. However, since the vector Laplacian satisfies

$$\nabla^2 \phi = \nabla (\nabla \cdot \phi) - \nabla \times (\nabla \times \phi), \quad (\text{S5})$$

we can write the equations of motion as

$$\mu \nabla \times (\nabla \times \phi) - (\lambda + 2\mu) \nabla (\nabla \cdot \phi) = -2 \frac{\partial V}{\partial \phi}. \quad (\text{S6})$$

This separates the rotational and volumetric components on the left-hand side.

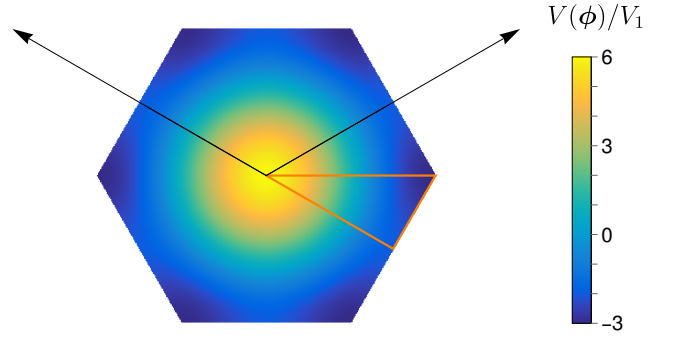


FIG. S1. Adhesion potential with C_{6v} symmetry in the first-star approximation versus the stacking configuration $\phi = (\phi_x, \phi_y)$. Arrows are monolayer primitive lattice vectors and the orange triangle contains all independent configurations.

In the first-star approximation, the stacking-fault energy for C_{6v} stacking symmetry is given by

$$V(\phi) = V_0 + 2V_1 \sum_{i=1}^3 \cos(\mathbf{b}_i \cdot \phi), \quad (\text{S7})$$

with V_0, V_1 real constants and where \mathbf{b}_i are the shortest nonzero reciprocal vectors of the monolayer that are related by threefold rotations. Since only derivatives of $V(\phi)$ appear in the equations of motion, we set $V_0 = 0$ from now on (as we do in the main text). The stacking-fault energy is shown in Fig. S1. We proceed to solve the equations of motion for a single isolated domain wall for both cases: $V_1 > 0$ and $V_1 < 0$. In particular, we consider two semi-infinite domains with translational symmetry along the direction of the domain wall. We then consider the full problem for a moiré bilayer where we solve the equations of motion numerically in Fourier space using

the self-consistent method implemented in JULIA in conjunction with the DIIS method (direct inversion of the iterative subspace).

A. AB/BA domain walls

We first consider the case $V_1 > 0$. We take a domain wall located at $y = 0$ with translational symmetry along x that separates regions with AB ($y > 0$) and BA ($y < 0$) stacking. Hence $\phi = \phi(y)$ and the equations of motion

become

$$\begin{bmatrix} \mu\phi''_x \\ (\lambda + 2\mu)\phi''_y \end{bmatrix} = -4V_1 \sum_{i=1}^3 \mathbf{b}_i \sin(\mathbf{b}_i \cdot \phi), \quad (\text{S8})$$

where the primes indicate derivatives with respect to the y coordinate. In the coordinate system of Fig. 1 we can take $\mathbf{b}_1 = 4\pi\hat{x}/\sqrt{3}a$ and $\mathbf{b}_{2/3}$ related by C_{3z} . Setting $a = 1$ we explicitly have

$$\sum_{i=1}^3 \mathbf{b}_i \sin(\mathbf{b}_i \cdot \phi) = \frac{4\pi}{\sqrt{3}} \begin{pmatrix} \sin\left(\frac{2\pi\phi_x}{\sqrt{3}}\right) \left[\cos(2\pi\phi_y) + 2\cos\left(\frac{2\pi\phi_x}{\sqrt{3}}\right) \right] \\ \sin(2\pi\phi_y) \cos\left(\frac{2\pi\phi_x}{\sqrt{3}}\right) \end{pmatrix}. \quad (\text{S9})$$

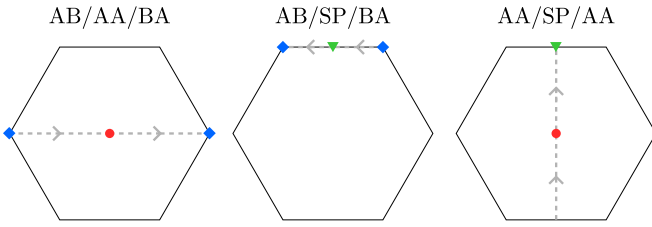


FIG. S2. Three domain walls shown in configuration space (the $\phi_x - \phi_y$ plane) as dashed lines where the arrows point from $-\infty$ to $+\infty$ in the direction perpendicular to the domain wall. The red dot, blue diamonds, and green triangle correspond to AA, AB/BA, and SP stacking, respectively.

We now consider two different types of pure shear domain walls, which are illustrated in Fig. S2. The first type is an AB/AA/BA interface with $\phi_y = 0$ and boundary conditions

$$\phi(y = \pm\infty) = \frac{1}{\sqrt{3}} \begin{pmatrix} \pm 1 \\ 0 \end{pmatrix} = \phi_{\text{AB/BA}}, \quad (\text{S10})$$

and the second one is an AB/SP/BA interface with $\phi_y = 1/2$ and boundary conditions

$$\phi(y = \pm\infty) = \frac{1}{\sqrt{3}} \begin{pmatrix} \mp \frac{1}{2} \\ \frac{\sqrt{3}}{2} \end{pmatrix} = \phi_{\text{AB/BA}}, \quad (\text{S11})$$

For both types of domain wall, the constant ϕ_y solves one of the equations in Eq. (S8). We are left with a second-order ordinary differential equation

$$\phi''_x + \frac{16c_1\pi}{\sqrt{3}} \left[\pm \sin\left(\frac{2\pi\phi_x}{\sqrt{3}}\right) + \sin\left(\frac{4\pi\phi_x}{\sqrt{3}}\right) \right] = 0, \quad (\text{S12})$$

with $c_1 = V_1/\mu$ and where \pm corresponds to the AA and SP domain wall, respectively. Defining $f = 2\pi\phi_x/\sqrt{3}$ and $t = y/w$, we obtain

$$f'' \pm \sin f + \sin 2f = 0, \quad (\text{S13})$$

with boundary conditions $f(t = \pm\infty) = \pm 2\pi/3$ and $f'(t = \pm\infty) = \mp \pi/3$, respectively. Here we defined

$$w = \frac{1}{4\pi} \sqrt{\frac{3}{2c_1}}. \quad (\text{S14})$$

Multiplying with $2f'$ and integrating gives

$$(f')^2 = A \pm 2 \cos f + \cos 2f, \quad (\text{S15})$$

where $A = 3/2$ from the boundary conditions. Here we also used that $f'(t = \pm\infty) = 0$. We obtain

$$f' = \frac{1 \pm 2 \cos f}{\sqrt{2}}, \quad (\text{S16})$$

where the sign is chosen to match the boundary conditions ($f' > 0$ for the AA domain wall and $f' < 0$ for the SP domain wall). The solutions take the form of a Gudermannian function

$$f_{\text{AA}}(y) = 2 \arctan \left[\sqrt{3} \tanh \left(\sqrt{\frac{3}{2}} \frac{y}{2w} \right) \right], \quad (\text{S17})$$

$$f_{\text{SP}}(y) = -2 \arctan \left[\frac{1}{\sqrt{3}} \tanh \left(\sqrt{\frac{3}{2}} \frac{y}{2w} \right) \right]. \quad (\text{S18})$$

We see that the slope of the AA domain wall is three times larger than that of the SP domain wall. Hence the AA soliton is more narrow than the SP soliton. This is to be expected since the energy barrier is 9 times larger for AA compared to SP stacking. We further note that our solution for the SP domain wall do not match the solution of Ref. [33] and we believe there is a minor arithmetical mistake in that work. While this does not change their conclusions, we observe that our solution matches the full numerical solution, see Fig. S3. The full width at

half maximum of the soliton is given by (in units a)

$$\delta y_{AA} = \frac{\ln(2)}{2\pi\sqrt{c_1}} \approx \frac{0.11}{\sqrt{c_1}}, \quad (\text{S19})$$

$$\delta y_{SP} = \frac{\ln(1 + \sqrt{3})}{2\pi\sqrt{c_1}} \approx \frac{0.16}{\sqrt{c_1}}. \quad (\text{S20})$$

For example, for twisted bilayer graphene using $c_1 \approx 4.5 \times 10^{-5}$ we have $\delta y_{SP} \approx 24$ and for twisted WSe₂ near 0° we have $c_1 \approx 3.9 \times 10^{-4}$ giving $\delta y_{SP} \approx 8$ [25]. However, these values slightly overestimate the domain wall width because of higher-order contributions to the adhesion potential as we discuss below.

We note that Eq. (S15) already suffices for our purposes since we are mainly interested in the slope of the domain wall. In this way, we only have to do one in-

tegration that remains straightforward when we include higher-order stars in the stacking-fault energy. For the SP domain wall, which is relevant for D_6 twist moirés, we obtain [24]

$$\phi'_x(0) = -2\sqrt{c_1 - 8c_2 + 9c_3}, \quad (\text{S21})$$

where $c_{2,3} = V_{2,3}/\mu$ are real coefficients belonging to the second and third star, respectively. For example, we know that for tTMDs, c_2 and c_3 are generally negative and about ten times smaller in magnitude than c_1 [20, 21]. However, because of the large prefactors in Eq. (S21) these contributions have a significant effect on the soliton size. Up to the third star, the stacking-fault energy for C_{6v} symmetry is given by

$$V(\phi) = 2V_1 \{ \cos(\mathbf{b}_1 \cdot \phi) + \cos(\mathbf{b}_2 \cdot \phi) + \cos[(\mathbf{b}_1 + \mathbf{b}_2) \cdot \phi] \} \quad (\text{S22})$$

$$+ 2V_2 \{ \cos[(\mathbf{b}_1 + 2\mathbf{b}_2) \cdot \phi] + \cos[(2\mathbf{b}_1 + \mathbf{b}_2) \cdot \phi] + \cos[(\mathbf{b}_1 - \mathbf{b}_2) \cdot \phi] \} \quad (\text{S23})$$

$$+ 2V_3 \{ \cos(2\mathbf{b}_1 \cdot \phi) + \cos(2\mathbf{b}_2 \cdot \phi) + \cos[2(\mathbf{b}_1 + \mathbf{b}_2) \cdot \phi] \}. \quad (\text{S24})$$

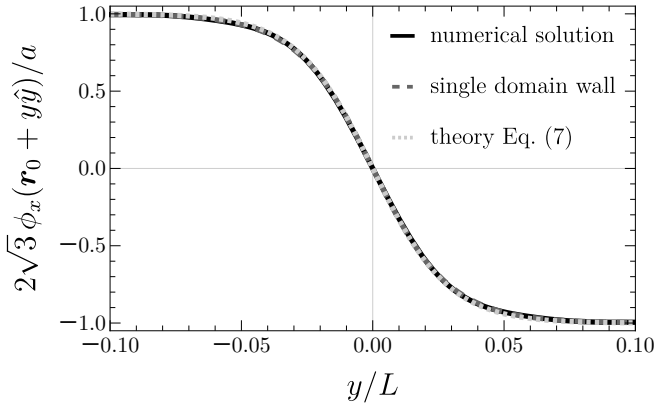


FIG. S3. AB/SP/BA domain wall of the triangular network ($V_1 > 0$) comparing the numerical solution for the full moiré from continuum elasticity to the analytical result for a single domain wall, and the theory in Eq. (5) of the main text.

We show the solution for the isolated single AB/SP/BA domain wall in Fig. S3. Here we also show the numerical solution of continuum elasticity for the twist moiré, as well as the small-angle theory for $V_1 > 0$ that we present in the main text.

B. AA/SP/AA domain wall

We now consider $V_1 < 0$ and take a domain wall located at $x = 0$ with translational symmetry along y

that separates regions with AA stacking (full dislocation). Hence $\phi = \phi(x)$ and the equations of motion become

$$\begin{bmatrix} (\lambda + 2\mu) \phi''_x \\ \mu \phi''_y \end{bmatrix} = 2 \frac{\partial V}{\partial \phi}, \quad (\text{S25})$$

where the primes indicate derivatives with respect to the x coordinate. We now set $\phi_x = 0$ and take boundary conditions $f(t = +\infty) = 2\pi$ and $f(t = -\infty) = 0$ with $f = 2\pi\phi_y$. In the first-star approximation, this yields

$$f' - 2 \sin \frac{f}{2} = 0, \quad (\text{S26})$$

with solution

$$f(x) = 2 \arccos \left(-\tanh \frac{x}{w'} \right), \quad (\text{S27})$$

where

$$w' = \frac{1}{4\pi} \frac{1}{\sqrt{-2c_1}}, \quad (\text{S28})$$

with $c_1 = V_1/\mu < 0$. The full width at half maximum of the soliton is then given by (in units of a)

$$\delta x = \frac{\cosh^{-1}(3)}{4\pi\sqrt{-2c_1}} \approx \frac{0.1}{\sqrt{-c_1}}. \quad (\text{S29})$$

Up to the third star, the slope of the AA/SP/AA domain wall is given by

$$\phi'_y(0) = 4\sqrt{-2(c_1 + c_2)}, \quad (\text{S30})$$

with $c_2 = V_2/\mu$.

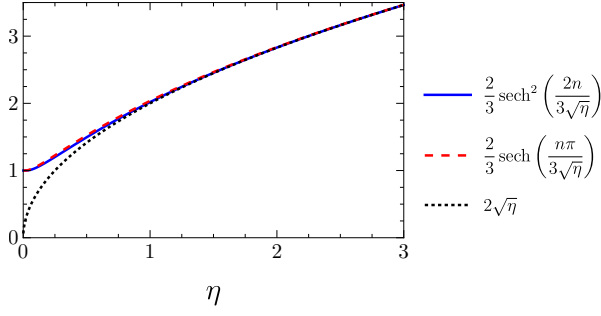


FIG. S4. Slope of the triangular soliton network [Eq. (S31)] for different parameterizations of $u_{n,0}^\perp$.

C. Soliton slope of triangular network

In the main text, we constrain the expression for the triangular soliton network by matching the slope of an isolated soliton:

$$2\sqrt{\eta} = 1 + \sum_{n=1}^{\infty} [2 + (-1)^n] u_{n,0}^\perp. \quad (\text{S31})$$

We find this is satisfied for $\eta \gg 1$ by

$$u_{n,0}^\perp = \frac{2}{3} \operatorname{sech}^2\left(\frac{2n}{3\sqrt{\eta}}\right). \quad (\text{S32})$$

Moreover,

$$u_{n,0}^\perp = \frac{2}{3} \operatorname{sech}\left(\frac{n\pi}{3\sqrt{\eta}}\right), \quad (\text{S33})$$

$$u_{n,0}^\perp = \frac{2}{3} \frac{n\pi^2}{6\sqrt{\eta}} \operatorname{csch}\left(\frac{n\pi^2}{6\sqrt{\eta}}\right), \quad (\text{S34})$$

give the same result for the slope, see Fig. S4. Presumably there is a whole family of exponentially decaying functions with similar properties such that they all satisfy Eq. (S31) in the limit $\eta \gg 1$. Here Eq. (S34) gives almost the same result as Eq. (S32) when it come to matching the soliton slope. They agree up to 0.1% so we do not show it in Fig. S4. We opted for Eq. (S32) because it fitted best to the LAMMPS molecular dynamics simulations for tWSe₂.

S2. NUMERICAL SOLUTION

The elastic and adhesion energy of a bilayer moiré material governing the disregistry are given by

$$F_{\text{elas}} = \int d^2\mathbf{r} \left[\frac{\lambda}{4} (\partial_i \phi_i)^2 + \frac{\mu}{8} (\partial_i \phi_j + \partial_j \phi_i)^2 \right], \quad (\text{S35})$$

$$F_{\text{adh}} = \int d^2\mathbf{r} V[\phi(\mathbf{r})], \quad (\text{S36})$$

where $\phi = M\mathbf{r} + \mathbf{u}_1 - \mathbf{u}_2$ is the interlayer disregistry. For a twist homobilayer, we have

$$\phi(\mathbf{r}) = \frac{a}{L} \hat{z} \times \mathbf{r} + \mathbf{u}(\mathbf{r}), \quad (\text{S37})$$

where

$$\mathbf{u}(\mathbf{r}) = \sum_{\mathbf{g}} \mathbf{u}_{\mathbf{g}} e^{i\mathbf{g} \cdot \mathbf{r}}, \quad (\text{S38})$$

is the acoustic displacement field with \mathbf{g} moiré reciprocal lattice vectors. Here we imposed moiré periodic boundary conditions and we set $\mathbf{u}_{\mathbf{g}=\mathbf{0}} = \mathbf{0}$ since it corresponds to an overall translation that only shifts the moiré lattice in the long-wavelength limit. We further have

$$\mathbf{b} \cdot \phi(\mathbf{r}) = \mathbf{g} \cdot \mathbf{r} + \mathbf{b} \cdot \mathbf{u}(\mathbf{r}), \quad (\text{S39})$$

where \mathbf{b} is a reciprocal lattice vector of the monolayer with $\mathbf{g} = M^T \mathbf{b} = \frac{a}{L} \mathbf{b} \times \hat{z}$. The total energy density $f = f_{\text{elas}} + f_{\text{adh}}$ then becomes

$$f_{\text{elas}} = \frac{a^2}{4L^2} \sum_{\mathbf{g}} \left[(\lambda + 2\mu) |u_{\mathbf{g}}^\parallel|^2 + \mu |u_{\mathbf{g}}^\perp|^2 \right], \quad (\text{S40})$$

$$f_{\text{adh}} = \frac{1}{A} \int_{\text{moiré cell}} d^2\mathbf{r} V[\phi(\mathbf{r})], \quad (\text{S41})$$

where $A = |\mathbf{L}_1 \times \mathbf{L}_2|$ is the moiré cell area and

$$u_{\mathbf{g}}^\parallel = \frac{iL}{a} \mathbf{g} \cdot \mathbf{u}_{\mathbf{g}}, \quad u_{\mathbf{g}}^\perp = \frac{iL}{a} (\hat{z} \times \mathbf{g}) \cdot \mathbf{u}_{\mathbf{g}}, \quad (\text{S42})$$

are (scaled) longitudinal and transverse components of the displacement field. Here we anticipate writing \mathbf{g} and \mathbf{u} in units of $1/L$ and a , respectively.

A. Self-consistent solution

The gradient of the energy with respect to the components is given by

$$\frac{\partial f}{\partial u_{-\mathbf{g}}^\parallel} = \frac{a^2}{2L^2} (\lambda + 2\mu) u_{\mathbf{g}}^\parallel + \frac{\partial f_{\text{adh}}}{\partial u_{-\mathbf{g}}^\parallel}, \quad (\text{S43})$$

$$\frac{\partial f}{\partial u_{-\mathbf{g}}^\perp} = \frac{a^2}{2L^2} \mu u_{\mathbf{g}}^\perp + \frac{\partial f_{\text{adh}}}{\partial u_{-\mathbf{g}}^\perp}, \quad (\text{S44})$$

with

$$\frac{\partial f_{\text{adh}}}{\partial u_{-\mathbf{g}}^\parallel} = \frac{1}{A} \int_{\text{moiré cell}} d^2\mathbf{r} \frac{\partial \mathbf{u}}{\partial u_{-\mathbf{g}}^\parallel} \cdot \frac{\partial V}{\partial \phi} \quad (\text{S45})$$

$$= -\frac{a}{L} \frac{\mathbf{g}}{ig^2} \cdot \left(\frac{\partial V}{\partial \phi} \right)_{\mathbf{g}}, \quad (\text{S46})$$

$$\frac{\partial f_{\text{adh}}}{\partial u_{-\mathbf{g}}^\perp} = -\frac{a}{L} \frac{\hat{z} \times \mathbf{g}}{ig^2} \cdot \left(\frac{\partial V}{\partial \phi} \right)_{\mathbf{g}}, \quad (\text{S47})$$

with

$$\frac{\partial V}{\partial \phi} = \sum_{\mathbf{b}} i\mathbf{b} V_{\mathbf{b}} e^{i\mathbf{b} \cdot \phi}. \quad (\text{S48})$$

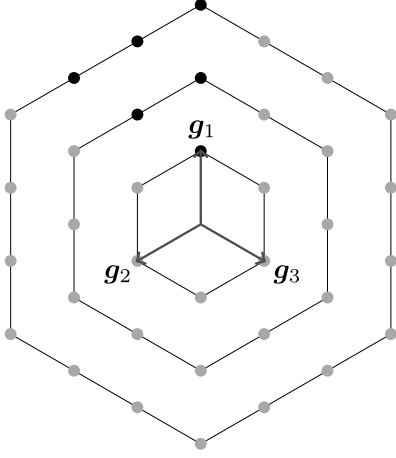


FIG. S5. The first three reciprocal shells where we omit the zeroth shell, i.e., the origin. Each shell corresponds to the reciprocal vectors (points) that lie on a hexagon. These are further divided into reciprocal stars that are closed under 60° rotations: the n th shell contains n stars. Here the black dots give one choice of representatives, while the gray dots give reciprocal vectors related by symmetry.

Hence, the self-consistency equations are given by

$$u_{\mathbf{g}}^{\parallel} = \frac{2L^2}{a^2} \frac{\mathbf{g}}{Lg^2} \cdot \left(\frac{-ia}{\lambda + 2\mu} \frac{\partial V}{\partial \phi} \right)_{\mathbf{g}}, \quad (\text{S49})$$

$$u_{\mathbf{g}}^{\perp} = \frac{2L^2}{a^2} \frac{\hat{z} \times \mathbf{g}}{Lg^2} \cdot \left(\frac{-ia}{\mu} \frac{\partial V}{\partial \phi} \right)_{\mathbf{g}}. \quad (\text{S50})$$

In this work, we only consider moirés with C_{3z} symmetry such that we only need to solve for two complex coefficients $u_{n,m}^{\parallel}$ and $u_{n,m}^{\perp}$ for each reciprocal star. We define a star as a collection of six reciprocal vectors of equal length that are closed under C_{6z} rotations. The stars are grouped into shells where the n th reciprocal shell contains a total of n stars with $m = 0, \dots, n-1$. These correspond to the collection of reciprocal vectors that lie on the edges of a hexagon of radius $4\pi n/\sqrt{3}L$. This is illustrated in Fig. S5. Hence, we only need to choose one representative $\mathbf{g}_{n,m} = n\mathbf{g}_1 + m\mathbf{g}_2$ for each star. The

self-consistency equations are independent of the choice of representative because

$$\left(\frac{\partial V}{\partial \phi} \right)_{S\mathbf{g}} = S \left(\frac{\partial V}{\partial \phi} \right)_{\mathbf{g}}, \quad (\text{S51})$$

for a rotation symmetry S . The displacement field is then given by

$$\frac{\mathbf{u}(\mathbf{r})}{a} = 2\text{Re} \sum_{n=1}^{\infty} \sum_{m=0}^{n-1} \sum_{j=1}^3 \times C_{3z}^j \frac{u_{n,m}^{\parallel} \mathbf{g}_{n,m} + u_{n,m}^{\perp} \hat{z} \times \mathbf{g}_{n,m}}{iLg_{n,m}^2} e^{iC_{3z}^j \mathbf{g}_{n,m} \cdot \mathbf{r}}. \quad (\text{S52})$$

The parameters of this theory are given by λ/μ and $\eta_i = (L^2/a^2)V_i/\mu$.

B. Perturbation theory

In lowest order of $|\mathbf{u}(\mathbf{r})/a|$ we can set the displacement field to zero on the right-hand side of Eqs. (S49) and (S50). This yields the one-shot result:

$$u_{\mathbf{g}}^{\parallel} \simeq \frac{2L^2}{a^2} \frac{\mathbf{g} \cdot \mathbf{b}}{Lg^2} \frac{aV_{\mathbf{g}}}{\lambda + 2\mu}, \quad (\text{S53})$$

$$u_{\mathbf{g}}^{\perp} \simeq \frac{2L^2}{a^2} \frac{(\hat{z} \times \mathbf{g}) \cdot \mathbf{b}}{Lg^2} \frac{aV_{\mathbf{g}}}{\mu}, \quad (\text{S54})$$

with $\mathbf{b} = \frac{L}{a} \hat{z} \times \mathbf{g}$ such that in lowest order

$$u_{\mathbf{g}}^{\parallel} = 0, \quad u_{\mathbf{g}}^{\perp} = \frac{2L^2}{a^2} \frac{V_{\mathbf{g}}}{\mu} = 2\eta_{\mathbf{g}}. \quad (\text{S55})$$

Alternatively, we can expand the adhesion energy S41 up to first-order in the displacement field [25]. This allows for a more systematic perturbative expansion. Noting that

$$V[\phi(\mathbf{r})] = \sum_{\mathbf{g}} V_{\mathbf{g}} e^{i\mathbf{g} \cdot \mathbf{r}} e^{i\mathbf{g} \cdot M^{-1} \mathbf{u}(\mathbf{r})}, \quad (\text{S56})$$

we have

$$f_{\text{adh}} = \frac{1}{A} \sum_{\mathbf{g}} V_{\mathbf{g}} \int d^2\mathbf{r} e^{i\mathbf{g} \cdot \mathbf{r}} \left\{ 1 + i\mathbf{g} \cdot M^{-1} \mathbf{u}(\mathbf{r}) - \frac{1}{2} [\mathbf{g} \cdot M^{-1} \mathbf{u}(\mathbf{r})]^2 + \dots \right\} \quad (\text{S57})$$

$$= V_0 + \sum_{\mathbf{g}} V_{\mathbf{g}} (i\mathbf{g} \cdot M^{-1} \mathbf{u}_{-\mathbf{g}}) - \frac{1}{2} \sum_{\mathbf{g}} V_{\mathbf{g}} \sum_{\mathbf{g}' \neq \mathbf{g}} (\mathbf{g} \cdot M^{-1} \mathbf{u}_{-\mathbf{g}'}) (\mathbf{g} \cdot M^{-1} \mathbf{u}_{\mathbf{g}'-\mathbf{g}}) + \dots. \quad (\text{S58})$$

We can systematically perform this expansion given an *ansatz* for $\mathbf{u}(\mathbf{r})$ by simply expanding the integrand in Mathematica and selecting terms that do not depend on the coordinates. For twist moirés, we have $M^{-1} \mathbf{u}_{\mathbf{g}} = (L/a) \mathbf{u}_{\mathbf{g}} \times \hat{z}$ and we obtain

$$f_{\text{adh}} = V_0 - \sum_{\mathbf{g}} V_{\mathbf{g}} u_{-\mathbf{g}}^{\perp} - \frac{L^2}{2a^2} \sum_{\mathbf{g}} V_{\mathbf{g}} \sum_{\mathbf{g}' \neq \mathbf{g}} (\hat{z} \times \mathbf{g} \cdot \mathbf{u}_{-\mathbf{g}'}) (\hat{z} \times \mathbf{g} \cdot \mathbf{u}_{\mathbf{g}'-\mathbf{g}}) + \dots. \quad (\text{S59})$$

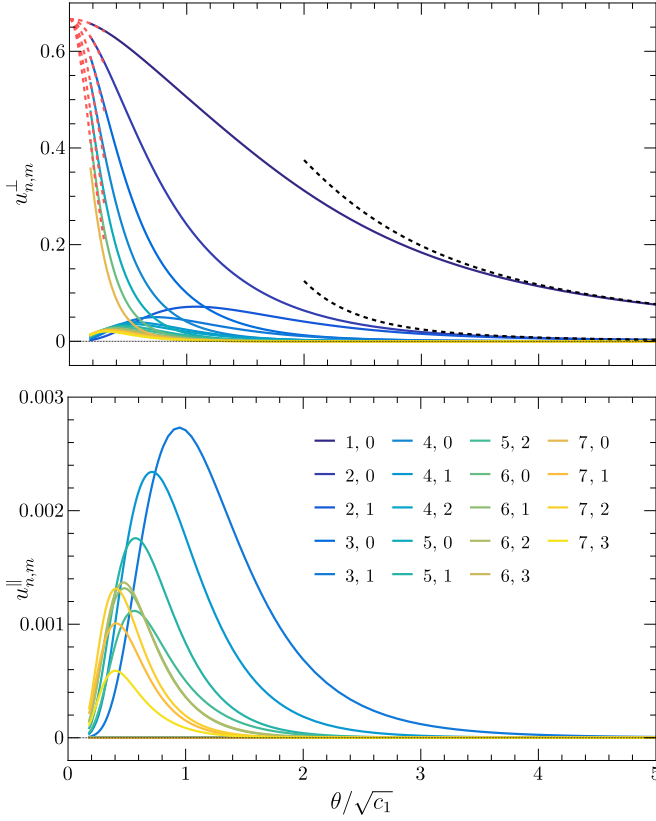


FIG. S6. Numerical solution for $V_1 > 0$ as a function of $1/\sqrt{\eta}$. We show distinct values not related by symmetry for the first 7 shells (28 stars). Note that the longitudinal components are more than two orders of magnitude smaller and are maximal in the intermediate regime $\eta \approx 1$. For the transverse components, the dashed lines give the perturbative result for “large” angles (black) and the *ansatz* for “small” angles.

One could also have used the Jacobi-Anger identity,

$$\begin{aligned} V[\phi(\mathbf{r})] &= \sum_{\mathbf{g}} V_{\mathbf{g}} e^{i\mathbf{g}\cdot\mathbf{r}} e^{i\mathbf{g}\cdot M^{-1}\sum_{\mathbf{g}'} i\mathbf{u}_{\mathbf{g}'} \sin(\mathbf{g}'\cdot\mathbf{r})} \quad (\text{S60}) \\ &= \sum_{\mathbf{g}} V_{\mathbf{g}} e^{i\mathbf{g}\cdot\mathbf{r}} \\ &\times \prod_{\mathbf{g}'} \sum_{m=-\infty}^{\infty} J_m(\mathbf{g}\cdot M^{-1}i\mathbf{u}_{\mathbf{g}'}) e^{im\mathbf{g}'\cdot\mathbf{r}}, \quad (\text{S61}) \end{aligned}$$

to expand the adhesion energy in an infinite series of Bessel functions [26, 27]. However, since in the end analytical progress can only be made by expanding the adhesion energy, we prefer to directly expand it in powers of $|\mathbf{u}/a|$.

For example, if we only include the first three stars, we only have to consider three transverse components $u_1 = u_{1,0}^\perp$, $u_2 = u_{2,1}^\perp$, and $u_3 = u_{2,0}^\perp$ because the longitudinal components are forbidden by D_6 symmetry. Up to third order, including also three stars for the adhesion potential, we obtain

$$f_{\text{elas}} = \frac{3\mu}{2} \frac{a^2}{L^2} (u_1^2 + u_2^2 + u_3^2), \quad (\text{S62})$$

and (ignoring the constant term V_0) up to third order in $|\mathbf{u}/a|$ we find

$$f_{\text{adh}} = V_1 \left\{ \frac{3}{8} [8u_1(2u_1^2 + u_1u_2 + u_2^2) + 2u_2u_3(3u_1 + 2u_2) + 7u_1u_3^2] + \frac{3}{2}u_1[u_1 - 2(u_2 + u_3)] - 6u_1 \right\} \quad (\text{S63})$$

$$+ V_2 \left\{ \frac{3}{8} [16u_2^3 + 36u_1u_2u_3 + 27u_2u_3^2 + 18u_1^2(4u_2 + 3u_3)] + \frac{3}{2}(9u_1^2 + u_2^2) - 6u_2 \right\} \quad (\text{S64})$$

$$+ V_3 \left\{ 3[-4u_1^3 + 5u_2^2u_3 + 2u_3^3 + 2u_1u_2(2u_2 + u_3) + u_1^2(8u_2 + 11u_3)] + \frac{3}{2}[8u_1(u_1 + u_2) + u_3^2] - 6u_3 \right\}. \quad (\text{S65})$$

This then yields three equations ($i = 1, 2, 3$)

$$\frac{\partial}{\partial u_i} (f_{\text{elas}} + f_{\text{adh}}) = 0, \quad (\text{S66})$$

which are solved perturbatively using the Frobenius method by expanding each u_i in powers of $\eta_j =$

$(L^2/a^2)V_j/\mu \approx V_j/(\theta^2\mu)$ ($j = 1, 2, 3$). We find

$$u_1 \approx 2\eta_1 - 2[\eta_1(\eta_1 + 8\eta_2 + 7\eta_3) + 4\eta_2\eta_3], \quad (\text{S67})$$

$$u_2 \approx 2\eta_2 + 2(\eta_1^2 - \eta_2^2 - 4\eta_1\eta_3), \quad (\text{S68})$$

$$u_3 \approx 2\eta_3 + 2(\eta_1^2 - \eta_3^2), \quad (\text{S69})$$

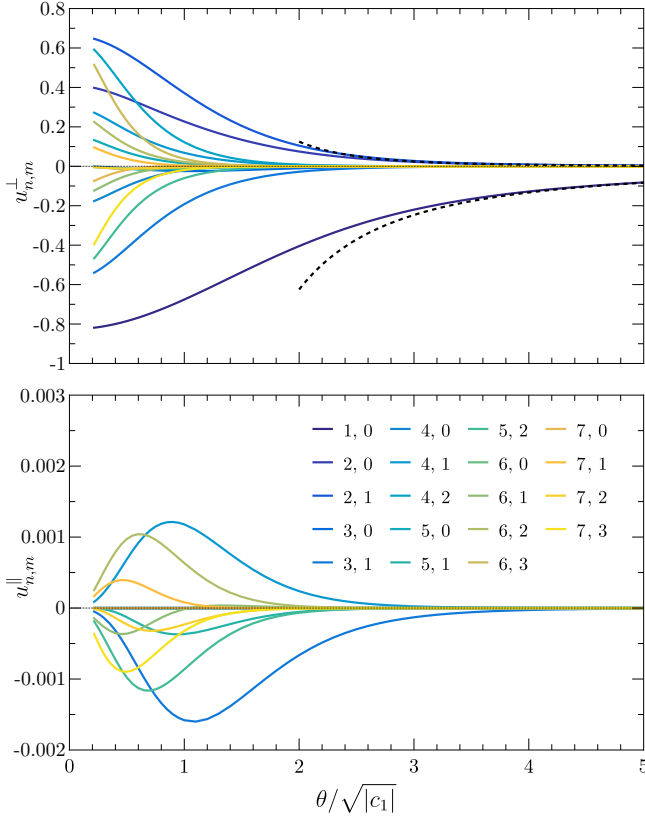


FIG. S7. Numerical solution for $V_1 < 0$ as a function of $1/\sqrt{|\eta|}$. We show distinct values not related by symmetry for the first 7 shells (28 stars). Note that the longitudinal components are more than two orders of magnitude smaller and are maximal in the intermediate regime $\eta \approx -1$.

or

$$u_{1,0}^\perp \approx \frac{2c_1}{\theta^2} - \frac{2[c_1(c_1 + 8c_2 + 7c_3) + 4c_2c_3]}{\theta^4}, \quad (\text{S70})$$

$$u_{2,1}^\perp \approx \frac{2c_2}{\theta^2} + \frac{2(c_1^2 - c_2^2 - 4c_1c_3)}{\theta^4}, \quad (\text{S71})$$

$$u_{2,0}^\perp \approx \frac{2c_3}{\theta^2} + \frac{2(c_1^2 - c_3^2)}{\theta^4}. \quad (\text{S72})$$

Here the dimensionless constants $c_i = V_i/\mu$ can be obtained by fitting the large twist angle scaling behavior to *ab initio* methods [25]. We compare our perturbative result to a recent paper [27]. We find that by going to third order for all three stars, we obtain $2\alpha = 1 + 8c_2/c_1 + 7c_3/c_1 \approx 0.05$ using the parameters for twisted bilayer graphene of Ref. [20].

C. First-star theory

If we restrict the stacking-fault energy to the first star, then it only depends on two real parameters $c = c_1$ and $\psi = \psi_1$. In this case, we define $\eta = \sqrt{c}L/a$. We see that for $\eta \ll 1$ we obtain Eq. (3) with $u_m^\perp = 2\eta^2 e^{i\psi} \delta_{m1}$

n, m	$u_{n,m}^\parallel$	$u_{n,m}^\perp$	n, m	$u_{n,m}^\parallel$	$u_{n,m}^\perp$
1, 0	0	\mathbb{R}	1, 0	0	\mathbb{C}
2, 1	0	\mathbb{R}	2, 1	$i\mathbb{R}$	\mathbb{R}
2, 0	0	\mathbb{R}	2, 0	0	\mathbb{C}
3, 1	\mathbb{R}	\mathbb{R}	3, 1	\mathbb{C}	\mathbb{C}
3, 2	$-u_{3,1}^\parallel$	$u_{3,1}^\perp$	3, 2	$-(u_{3,1}^\parallel)^*$	$(u_{3,1}^\perp)^*$

TABLE S1. Symmetry-allowed values for the in-plane and out-of-plane Fourier coefficients of the displacement fields in the presence of D_6 (left) and $D_3 = \langle \mathcal{C}_{3z}, \mathcal{C}_{2y} \rangle$ (right) symmetry for the first five reciprocal stars.

and $u_m^\parallel = 0$. For $\eta \gtrsim 1$, we solve the self-consistency equations numerically. Writing \mathbf{g} in units of $1/L$, $\partial V/\partial \phi$ in units of V_1/a , and λ in units of μ , we have

$$u_{\mathbf{g}}^\parallel = 2\eta^2 \frac{\mathbf{g}}{g^2} \cdot \left(\frac{-i}{\lambda + 2} \frac{\partial V}{\partial \phi} \right)_{\mathbf{g}}, \quad (\text{S73})$$

$$u_{\mathbf{g}}^\perp = 2\eta^2 \frac{\hat{z} \times \mathbf{g}}{g^2} \cdot \left(-i \frac{\partial V}{\partial \phi} \right)_{\mathbf{g}}. \quad (\text{S74})$$

Some results for large η are shown in Fig. S8. These results are all consistent with a symmetry analysis for D_6 twist moirés [25] shown in Table S1. Longitudinal components $u_{\mathbf{g}}^\parallel$ are only allowed in pairs of opposites corresponding to two stars that map into each other under \mathcal{C}_{2x} . Hence they vanish for any star that is closed under this symmetry. We also see that the magnitude of $u_{\mathbf{g}}^\parallel$ decays with increasing η . Moreover, the largest $|u_{\mathbf{g}}^\parallel|$ is almost three orders of magnitude smaller than the largest $|u_{\mathbf{g}}^\perp|$.

If we consider two different materials with different c then we expect the same relaxation physics for

$$\frac{\theta'}{\theta} = \sqrt{\frac{c'}{c}}. \quad (\text{S75})$$

For example, for group VI twisted bilayer 2H TMDs such as tWSe₂ and tMoTe₂: $c \sim 10 \times c_{\text{tBG}}$ such that we expect similar moiré reconstruction as compared to tBG for twist angles that are about a factor 3 larger [20, 21, 25].

Numerical implementation

We solve the self-consistency equations numerically in JULIA. In the numerical implementation we take a finite number of shells N giving a total number of stars $M = N(N+1)/2$ with representatives \mathbf{g}_m ($m = 1, \dots, M$). A configuration can then be defined by the longitudinal U^\parallel and transverse U^\perp components with

$$U^\parallel = \begin{pmatrix} u_1^\parallel \\ u_2^\parallel \\ \vdots \\ u_M^\parallel \end{pmatrix}, \quad U^\perp = \begin{pmatrix} u_1^\perp \\ u_2^\perp \\ \vdots \\ u_M^\perp \end{pmatrix}, \quad (\text{S76})$$

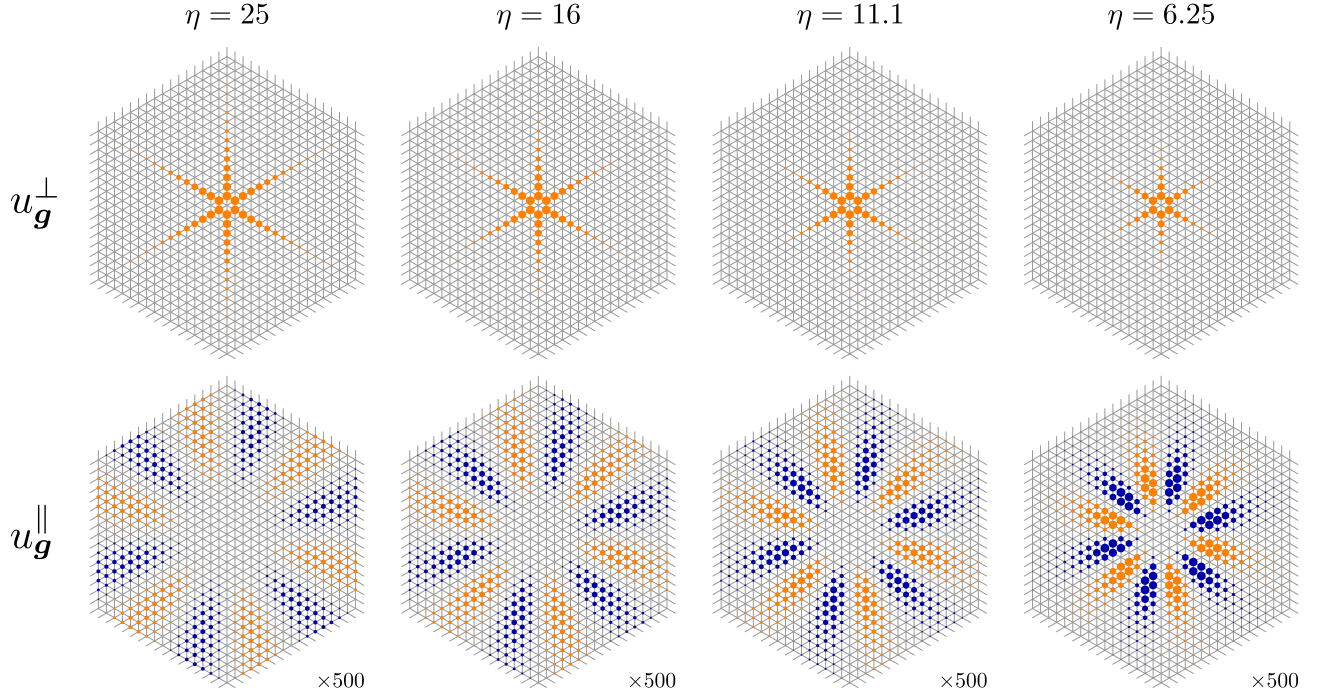


FIG. S8. Solution of continuum elasticity for a D_6 twist moiré in the first-star approximation with $V_1 > 0$ and $\lambda = 0$, showing 16 shells (136 stars). Here the dot size gives the magnitude of the Fourier components and the color indicates the sign, where orange (blue) is positive (negative). The longitudinal components u_g^{\parallel} are scaled by a factor 500.

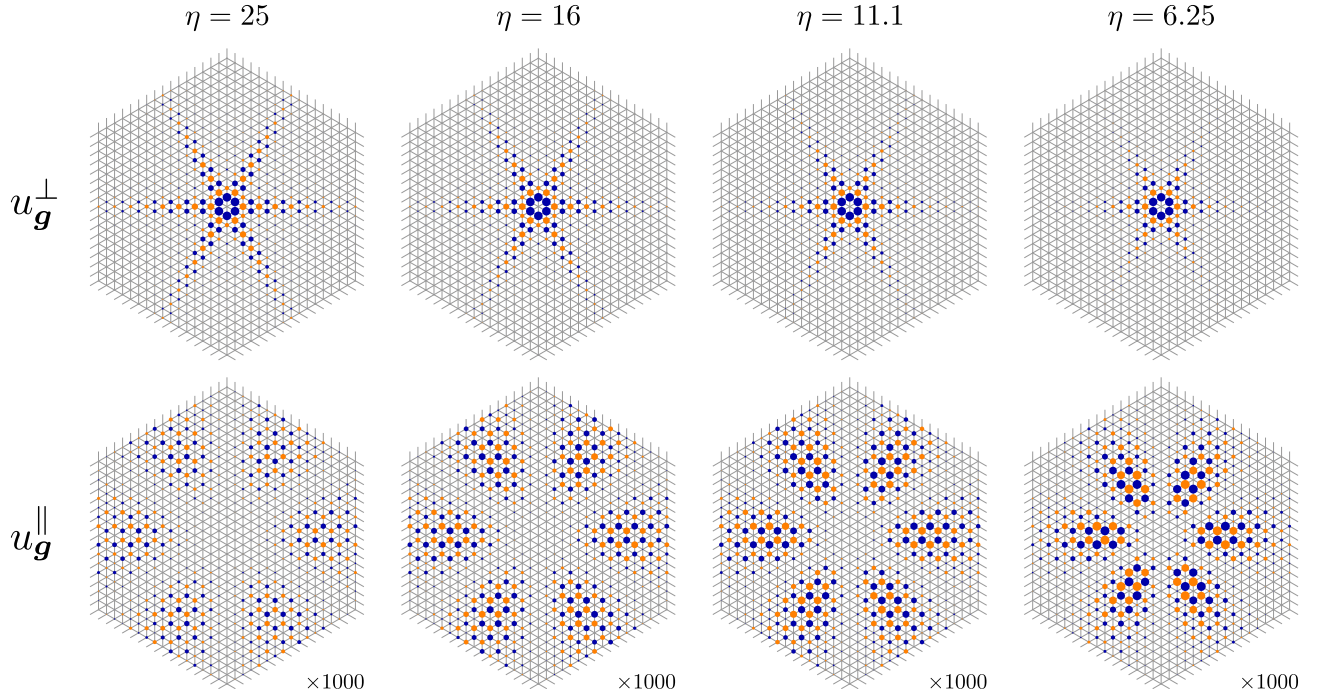


FIG. S9. Solution of continuum elasticity for a D_6 twist moiré in the first-star approximation with $V_1 < 0$ and $\lambda = 0$, showing 16 shells (136 stars). Here the dot size gives the magnitude of the Fourier components and the color indicates the sign, where orange (blue) is positive (negative). The longitudinal components u_g^{\parallel} are scaled by a factor 1000.

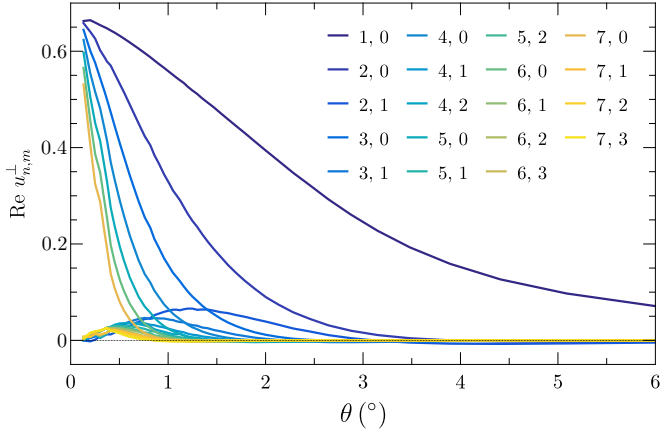


FIG. S10. Real part of transverse Fourier components for tWSe₂ near 0° (parallel stacking) calculated from LAMMPS simulations. We do not show the imaginary part and the longitudinal components because they are over two orders of magnitude smaller. Only distinct values not related by symmetry are shown for the first 7 shells (28 stars).

from which one can construct $\mathbf{u}(\mathbf{r})$. In fact, one can roughly half the number of stars further by taking into account \mathcal{C}_{2x} symmetry, see for example Table S1 for the fourth and fifth star. However, in practice we only take into account \mathcal{C}_{6z} symmetry which makes all coefficients real. We proceed by calculating the right-hand side of Eq. (S49) and Eq. (S50) numerically by computing M integrals in parallel. To avoid convergence issues, instead of directly updating the u_m^{\parallel} and u_m^{\perp} , we use the DIIS method (direct inversion of the iterative subspace) which was originally developed for the self-consistent field method [45, 46]. To further stabilize the algorithm, we always start in the perturbative regime $\eta \ll 1$ (large twist angles) where the exact solution is known and the solution converges quickly. Since the solution should be continuous as a function of η (or the twist angle), we gradually increase η (lower the twist angle), using the converged result of the previous larger angle as the starting point for the new smaller angle. Similarly, one can increase the number of shells N between consecutive runs. For our purposes we use $N = 18$. To make sure the results are converged properly, we always check whether the constraints from \mathcal{C}_{2x} symmetry are satisfied.

S3. LAMMPS MOLECULAR DYNAMICS SIMULATIONS

In the regime of marginal twist angles, the moiré lattice of a twisted 2H TMD homobilayer contains $6/\theta^2$ atoms, e.g., about 3×10^5 for $\theta = 0.25^\circ$. In this regime first-

principle calculations are prohibitively expensive. Therefore we model atomic relaxation with molecular dynamics simulations using the Large-scale Atomic/Molecular Massively Parallel Simulator (LAMMPS) code which employs classical interatomic force field models [18]. While these molecular dynamics simulations allow for larger supercell sizes, they have inherent limitations on accuracy over the choice of interatomic potentials. In our experience, while different interatomic potentials might give slightly different numerical values for the $c_i = V_i/\mu$ parameters, their qualitative behavior and symmetry properties are identical.

For tWSe₂ we use the Kolmogorov–Crespi potential for interlayer interactions [17] and the Stillinger–Weber (SW) potential for intralayer interactions with SW/mod style [47]. In this work, we performed relaxation calculations for commensurate twist angles ranging from $\theta = 0.1^\circ$ to $\theta = 10^\circ$. The smallest twist angles correspond to moiré cells with over one million atoms. Despite the large number of atoms in the simulation cell, the structural optimization remains computationally tractable due to the low cost of the classical potentials.

To compare with continuum elasticity which only describes acoustic degrees of freedom, we first extract the center-of-mass motion:

$$\mathbf{u}_l = \sum_i \frac{m_i}{M} \mathbf{u}_{li}, \quad (\text{S77})$$

for each layer $l = 1, 2$. Here $M = \sum_i m_i$ and the sum runs over atoms in the monolayer unit cell. For TMDs MX₂, we obtain

$$\mathbf{u}_l = \frac{m_M}{M} \mathbf{u}_{l,M} + \frac{m_X}{M} (\mathbf{u}_{l,X1} + \mathbf{u}_{l,X2}) \quad (\text{S78})$$

with $M = m_M + 2m_X$. For WSe₂ we use $m_W/M = 0.538$ and $m_{Se}/M = 0.231$ and for MoTe₂ with the data of Ref. [35] we use $m_{Mo}/M = 0.273$ and $m_{Te}/M = 0.363$.

In Figs. S10 and S11 we show the transverse Fourier components of the interlayer acoustic displacement field $\mathbf{u} = \mathbf{u}_1 - \mathbf{u}_2$ for twist angles near 0° and 60°, respectively. For twist angles near 0° (parallel stacking) the stacking symmetry is only approximately given by D_6 such that there is a small imaginary part. However, because the latter is over two orders of magnitude smaller, we do not show it. Similarly the longitudinal part is almost three orders of magnitude smaller. On the other hand, for twist angles near 60° (antiparallel stacking) the stacking symmetry is given by D_3 and the imaginary transverse component is significant in general. Only for marginal twist angles, does the imaginary component vanish as the honeycomb soliton network recovers the D_6 symmetry.

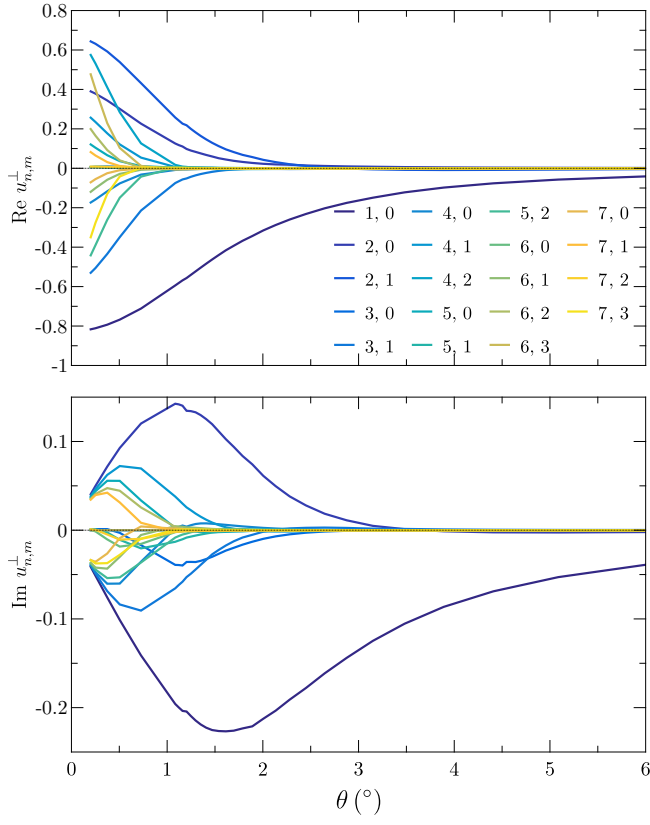


FIG. S11. Transverse Fourier components for tWSe₂ near 60° (antiparallel stacking) calculated from LAMMPS simulations. Here the total twist angle is 60° + θ . We do not show the longitudinal components because they are over two orders of magnitude smaller. Only distinct values not related by symmetry are shown for the first 7 shells (28 stars).